Journal of Sol-Gel Science and Technology (2024) 111:475–485
https://doi.org/10.1007/s10971-024-06470-1

ORIGINAL PAPER

Hard and soft templating approaches in evaporative sol-gel synthesis of $TiNb_2O_7$ nanostructures as active materials for Li-ion batteries

A. R. Rahmani[1] · M. Khodaei[1,2,3]

Received: 26 December 2023 / Accepted: 26 June 2024 / Published online: 6 July 2024

Abstract

As a promising alternative anode material for Li-ion batteries, monoclinic titanium niobate ($TiNb_2O_7$) offers the inherent safety associated with high lithiation potential combined with gravimetric capacities compared to that of graphite. Herein, evaporative sol-gel method has been employed to obtain $TiNb_2O_7$ with tailored morphology and crystallite structures. Using F127 co-polymer as structure directing soft template, the otherwise irregular morphology of the ceramic after calcination turns into an intricate assembly of interconnected particles with appropriately sized morphological voids for electrolyte contact and damping of the volumetric changes associated with lithiation process. Using cellulose as hard template will in turn increase the size scale of the interconnected particulates and associated morphological voids and enhances the crystallite characteristics known to enhance lithium diffusion and storage. The samples under study were subjected to high-resolution transmission electron microscopy, field-emission scanning electron microscopy, powder X-ray diffraction, selected area electron diffraction, Fourier transform infrared spectroscopy, diffuse reflectance spectroscopy and electrochemical analysis based on half-cells with lithium metal as counter electrode. Electrochemical characterization of the representative samples under study clearly shows a delicate balance between material characteristics which should simultaneously satisfy strict conditions for optimized performance. The optimized sample shows an initial Columbic efficiently of 99.2% at 0.1 C and cyclable capacity of 155 $mAhg^{-1}$ with a 76% retention upon 100 cycles of charge-discharge.

Graphical Abstract

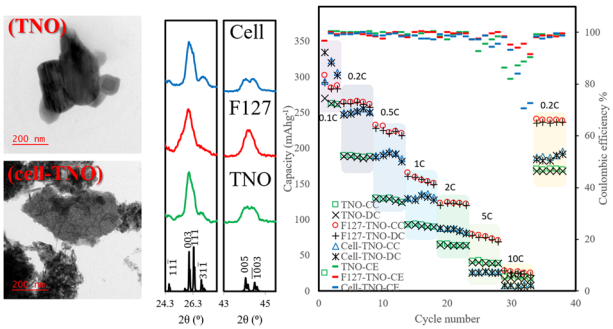

Keywords Hard-templating · Cellulose · F127 · TNO · Li-ion battery

✉ M. Khodaei
khodaei@kntu.ac.ir

[1] Faculty of Materials Science and Engineering, K. N. Toosi University of Technology, Tehran, Iran

[2] Advanced Materials and Nanotechnology Research Lab, Faculty of Materials Science and Engineering, K. N. Toosi University of Technology, Tehran, Iran

[3] Materonics and Materionics Research Group, K. N. Toosi University of Technology, Tehran, Iran

Highlights

- Evaporative sol-gel approach was taken as the synthesis method for nanostructured $TiNb_2O_7$
- F127 as a triblock co-polymer non-ionic surfactant was chosen as a representative soft-template.
- Microcrystalline cellulose was picked as a representative hard template
- All of the samples were characterized in terms of crystallography, morphology and performance in battery half-cells against lithium metal.
- The optimized sample showed an initial Columbic efficiently of 99.2% at 0.1C and cyclable capacity of 155 $mAhg^{-1}$ with a 76% retention upon 100 cycles of charge-discharge.

1 Introduction

Ever increasing global demand for energy and growing environmental awareness necessitate a significant leap forward in the field of renewable energy technologies. The intermittent nature of most renewable sources and functional aspects of mobility applications have caused the devotion of considerable efforts to lithium-ion battery technology amongst various energy storage options [1]. Traditionally, carbonous materials are utilized as active anode material in lithium-ion batteries [2]. Offering a theoretical capacity of 372 $mAhg^{-1}$, graphite has a lithiation potential of about 0.2 V *vs.* Li^+/Li^0 redox reaction potential which is favored as anode material; however, this feature becomes a double-edged sword especially at higher current densities which are vital for electric vehicle applications [3]. In such traditional anodes, instead of plating a smooth surface layer, lithium metal tends to form dendritic or mossy structures [4], which in turn may lead to catastrophic internal short circuiting of the cell [5].

High-voltage anode materials have been introduced to mitigate the aforementioned safety issues and enable high rate charge and discharge of the cell [6]. Lithium titanate spinel (so called LTO) with chemical formula of $Li_4Ti_5O_{12}$ has been the subject of considerable research efforts both in industry and academia [7]. This intercalation-type anode material offers a theoretical capacity of 175 mAg^{-1} with lithiation potential of 1.55 V *vs.* Li^+/Li^0; this potential corresponds to the Ti(IV)/Ti(III) redox couple. At this potential SEI layer formation is hindered, making this material a suitable anode for use at high rates for extended cycles of charge/discharge. Although, the inherently low capacity compared to graphite makes LTO an inferior candidate especially in terms of power density. A verity of approaches have been employed to enhance the performance of LTO; doping is considered as one of the main strategies in this area which has been recently reviewed by our team [8].

Introduced by Goodenough's research team [9], monoclinic $TiNb_2O_7$ (TNO) has a space group of C2/*m* and the so-called Wadsely-Roth phase consisting of ReO_3 like octahedra which share corners and exhibit shear planes at the boarders giving rise to $3 \times 3 \times \infty$ crystalline motifs [10] (Fig. 1a). In the phase diagram of TiO_2-Nb_2O_5 several ternary compounds can be found at the niobium-rich side, but the most titanium rich compound in this series is the $TiNb_2O_7$ [11]. Titanium and niobium ions in this structure are disordered and three redox pairs, Ti(IV)/Ti(III), Nb(V)/Nb(IV) and Nb(IV)/Nb(III) give rise to a considerable theoretical capacity of 387.6 $mAhg^{-1}$ which corresponds to ~5 lithium ion insertion per unit formula.

Challenges related to electrical and ionic conduction of TNO have triggered the devotion of tremendous research efforts in both the fundamental aspects [10, 12] and synthetic strategies including micro-and nano-structuring [13] and composite formation [14]. Several synthetic approaches have been taken to obtain and optimize the performance of TNO related materials including sol-gel [9], mechanochemical [10], solvothermal [15], blow spinning [16] and electrospinning [17]. Furthermore, different doping strategies have been reported to further optimize the electrochemical performance of TNO including vacuum annealing [18], self-doping (Nb-rich) [19] and doping with additional elements such as vanadium [20, 21], molybdenum [22, 23] and ruthenium [24].

Sol-gel has been one of the main strategies for the synthesis of high-quality TNO-based materials. Several approaches within the realm of sol-gel synthesis were reported for this material. One of the earliest approaches in this area has been to dissolve Nb_2O_5 in HF and then neutralize it into $Nb(OH)_5$ with ammonia which would further be dissolved with citric acid [9] or oxalic acid [25], then the titanium precursor in the form of titanium oxysulfate or tetrabutyl titanate is added in the intended stochiometric amount. Evaporation of the sol followed by calcination at high temperature would yield nanostructured TNO with varied microstructures based on the organic acid used in the process.

Rich morphological aspects can be induced in TNO-based nanostructures within sol-gel regime by using templating agents along with dissolvable niobium and titanium precursors. Soft templates which are already used for obtaining TNO include F127 [26, 27] and SDS [28]. While hard templates such as SBA-15 [29] and anodic alumina [30] have be go through post-calcination washing process, sacrificial ones including polystyrene dispersions [31] and DVB-*co*-VBC nanotubes [32] would burn out during the calcination step. Interestingly, both hard and soft templating approaches can also be employed at the same time for obtaining hierarchical nanostructures [33].

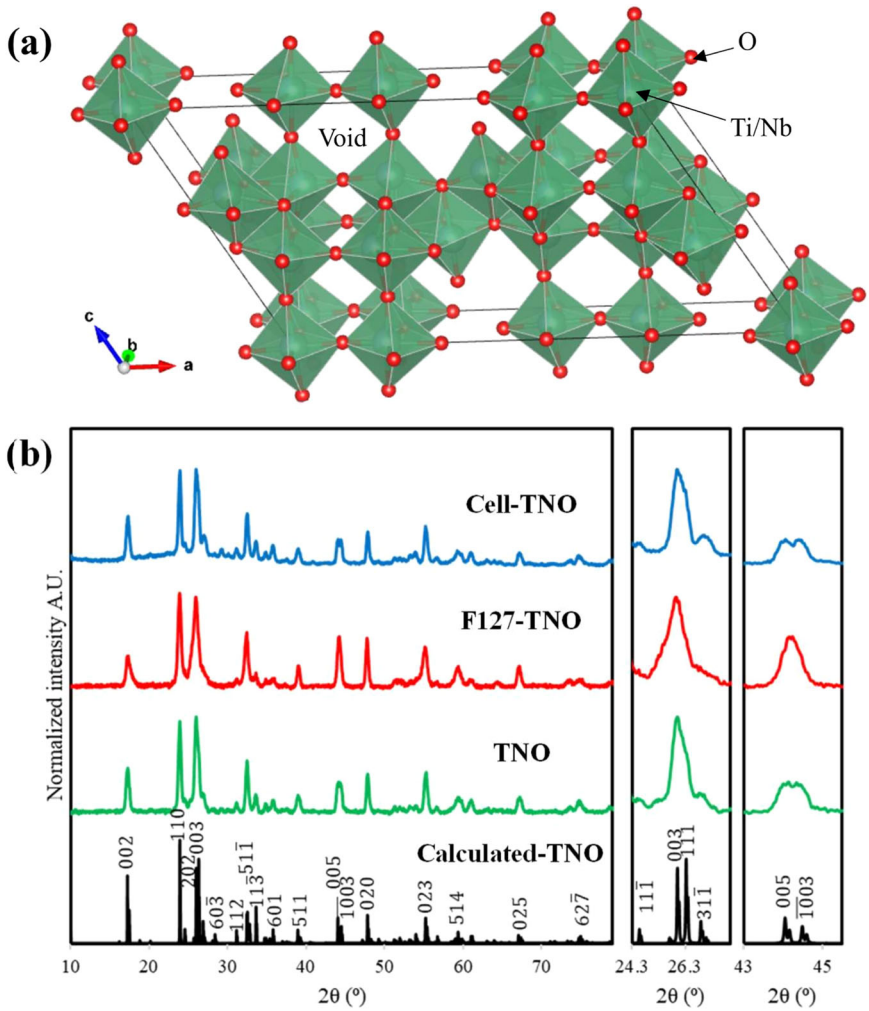

Fig. 1 **a** Crystal structure of $TiNb_2O_7$, **b** X-ray diffractograms of the samples under study along with standard pattern calculated from the crystal structure of $TiNb_2O_7$ and assigned based on JCPDS card no. 77-1374

In the current report, TNO was synthesized *via* evaporative sol-gel approach using cellulose as a sacrificial hard template, F127 copolymer as a soft one and without any templating agents for comparison. F127 is a triblock copolymer consisting a core block of poly (propylene oxide) surrounded by two tail chains of poly (ethylene oxide) giving it an approximate molecular weight of 12500 Daltons. Synthesized samples were characterized by phase and morphological techniques as well as electrochemical testing in half-cell configuration with lithium metal as counter electrode in order to represent the effect of hard and soft templating on the performance of TNO-based nanostructures obtained in sol-gel regime.

2 Experimental

2.1 Synthesis of TNO nanostructures

In order to obtain a clear solution containing both precursors of niobium and titanium in a 2:1 molar ratio (Nb:Ti), niobium pentachloride. $NbCl_5$ (98% Sigma-Aldrich, Germany) was weighted under an argon filled glovebox and kept in sealed microtubes. When needed, the seal would be broken under a chemical fume hood and the content was added to absolute ethanol (99.8% Kimia Alcohol Zanjan, Iran). A few drops of hydrochloric acid, HCl (37%, Ghatran Chime, Iran) are added to the aforementioned solution while being vigorously stirred until reaching a clear solution. This can effectively mitigate the formation of partial oxo-hydroxo-chloro complexes with the general stoichiometry of $NbCl_5–x(OC_2H_5)_x$ and other substituted species such as $Nb(OC_2H_5)_5$ which are formed otherwise when adding niobium pentachloride to absolute ethanol [34]. Afterwards, tetrabutyl titanate, $Ti(C_4H_9O)_4$ (97% Merck, Germany) was added dropwise to the ethanolic niobium solution. The obtained clear solution was sealed and kept in a desiccator under reduced pressure until further use. This solution was then aliquoted to be used in three separate experiments. The first aliquot was exposed to ambient conditions without further processing, to the second was added a weighted amount of F127 copolymer

Table 1 Brief summary of the samples under study

Sample code	Description
TNO	Original sol dried at ambient conditions without any kind of template or additive. Xerogel is obtained under these conditions after a few days.
F127-TNO	10 wt% (based on final mixed oxide) of F127 co-polymer was added to the sol precursor. Evaporation induced self-assembly (EIS) process was completed under ambient conditions during the course of several days.
Cell-TNO	Original sol precursor was wetted dropped on an excess amount of 5 mm wide tissue paper strips. Fully dry samples ready for calcination are obtained in the matter of few hours under ambient conditions.

(10 wt% based on the final mixed oxide) under stirring and then it was exposed to ambient conditions for evaporation induced self-assembly; the final part was dropped on stripes of tissue paper (5 mm wide) and left to be dried under ambient conditions. A brief description of aforementioned samples can be found in Table 1. All samples went through the same regime of heat treatment; they were first heated to 900 °C with a rate of 5°/min and a calcination dwelling time of 5 h, then annealed to room temperature overnight. Fired samples were finely grinded *via* agate mortar and pestle stored in desiccator under reduced pressure until further application.

2.2 Materials characterization

X-ray diffractograms were recorded from powdered samples on glass cells using a Rigaku (Japan) Ultima IV apparatus with CuK_α radiation in 2θ range of 10–80° with 0.02° step size. Phase content of the samples based on XRD patterns further was investigated using Rietveld refinement method performed with MAUD program [35]. XRD pattern calculation based on standard CIF file of $TiNb_2O_7$ was performed using VESTA program. The morphological features and elemental composition of the samples were studied through filed-emission scanning electron micrographs and energy-dispersive X-ray spectra on a TESCAN (Czech Republic) MIRA 3 microscope with 15 kV acceleration voltage using SE, BSE and EDS detectors. FTIR spectra of the samples were recorded in ATR mode using a Bruker (USA) Equinox 55 system. Diffuse reflectance spectra (DRS) were measured against barium sulfate as blank on a SCINCO (South Korea) S-4100 instrument. High resolution transmission electron micrographs and SAD patterns were obtained on a FEI (USA) Tecnai G2 F20 SuperTwin microscope using holey carbon copper grids and 200 KV accelerating voltage.

2.3 Electrochemical measurements

The synthesized samples were further studied in half-cell configuration against lithium metal. In order to obtain working electrodes for 2032 cells, dry and finely grinded powdered samples were made into slurries along with polyvinylidene fluoride (PVDF) (>99.5% MTI corp. China) as binder and super-P (MTI) as conductive agent in NMP solvent. The ratio of active material: binder: conductive agent was set at 80:10:10 for all experiments. Prepared slurries were coated onto copper foil (>99.8% MTI) using doctor blade apparatus and obtained assemblies were further dried under reduced pressure at 105 °C for 10 h. Surface density of about 1.5–2 mg/cm^2 was obtained for the electrodes after the drying procedure. The working electrodes were then punched and crimped into coin cells under dry argon atmosphere in a dedicated glove-box set-up. Other components of the half cells include lithium metal chips (>99.9 MTI), polypropylene membrane as separator and 1 M $LiPF_6$ dissolved in EC: DEC: DC (1:1:1 Vol. ratio) solvent (MTI) as electrolyte. Electrochemical measurements were conducted at 25 °C using a NEWARE (China) 4000 battery testing system at 0.8–3 V (*vs.* Li^+/Li^0) potential range.

3 Results and discussion

X-ray diffractograms obtained from powdered samples after calcination are presented in Fig. 1b. All diffraction patterns are in fair agreement with that of standards monoclinic $TiNb_2O_7$ (JCPDS no. 77-1374). Small un-indexed peaks may be related to titanium oxide phases (namely anatase and rutile) which were resolved using Rietveld refinement method; the calculated quantities of these impurity phases should be treated rather cautiously due to the limitation of normal powder XRD method in phase contents of such low amount.

As mentioned before, monoclinic TNO phase consists of randomly distributed Nb and Ti atoms (overall molar ratio of 2:1) each in coordination with six oxygen atoms forming ReO_3-like octahedra which share corners and edges to build up a long-range ordered structure. In this structure two features should be noted; first the crystalline void that can serve as host to intercalating lithium ions, thus, making it possible to host a significant number of intercalated lithium ions without compromising the structural integrity of the

crystal. This feature is vital for high rate and high-capacity performance of TNO especially when being subjected to extended cycling. With three possible redox couples, and suitable structural voids within the crystal it is possible for TNO to host even more than one lithium ion per transition metal atom (overlithiation) [10]. The second structural feature of monoclinic TNO phase is the two-dimensional channels along [100] and [010] directions which serve as migration pathways for lithium ions within the crystal which are interconnected with a tunnel in [001] direction [36].

The highest intensity peak of TNO phase is ideally located in $2\theta = 26^{\circ} \pm 0.5^{\circ}$ which is related to (003) crystalline plane, this peak is often inseparable from that of (111) plane due to similar interplanar distance between the two sets of planes, as can be seen for both "TNO" and "F127-TNO" samples in Fig. 1b. If the XRD peak related to (003) plane is indeed the most intense, the relative prevalence of this plane can be interpreted as preferential growth along [001] direction. Being the sole path of lithium migration between the fast channels of [100] and [010] directions, this type of growth is highly favorable for faster lithium diffusion within the crystal. Furthermore, this kind of growth expands the number of available structural voids which can effectively host intercalated lithium ions; thus, favoring both charge/discharge capacity and rate performance of the active material.

Another set of peaks appear at $2\theta = 44^{\circ} \pm 1^{\circ}$ which are related to (005) plane in the lower angle side and $(\overline{1}003)$ plane in the higher angle side. These peaks are also hard to distinguish and they may even appear inseparable as in the case of "F127-TNO" sample in Fig. 1b. In order for the material to show high lithium-ion diffusivity, the intensity of higher side peak in this couple should preferably be lower than that of the lower side peak [36]. This condition is met in the case of "TNO" sample but the exact opposite can be observed in the case of "Cell-TNO" sample. The prediction made by this criterion is further proved by rate performance of the samples under study which will be presented below.

DRS method was used to determine the absorbance photons in UV-Visible range against barium sulfate as blank to determine the optical band gap. The resulting curves of Fig. 2 clearly show a semiconducting behavior without any additional impurity bands due to templating agent. A distinct blue-shift is observed upon templating which is in agreement with the considerable decrease in crystallite sizes as mentioned in the part discussing XRD patterns and will be complemented with microscopic results next. In order to calculate the optical band gaps, Tauc plots were drawn (insert of Fig. 2) and extrapolated to the energy axis [37]. In modified Tauc plots, $(\alpha h\nu)^{1/r}$ is drawn against photon energy. In this function, α is the absorption

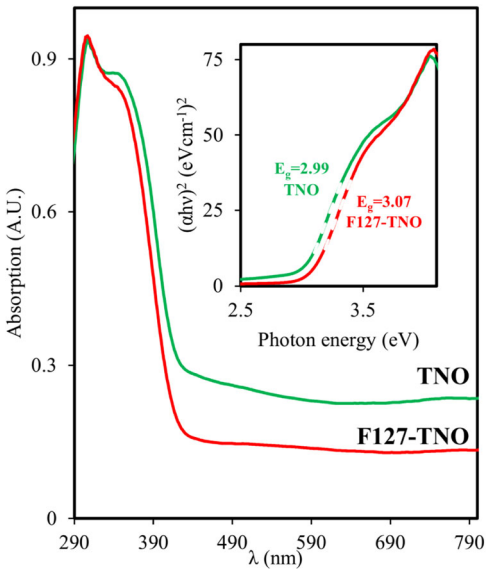

Fig. 2 Diffuse reflectance spectra of TNO and F127-TNO samples, the insert shows the Tauc plot and extrapolation of curves' shoulder gives the optical band gap assuming the electronic transition to be direct and allowed (r = 1/2)

coefficient of the material and the constant r is considered to be ½ for direct allowed electronic transitions [38].

In order to conclusively prove the successful removal of carbon containing templates (both F127 and cellulose), FTIR spectra in ATR mode were recorded for the samples under study; the results of which are presented in Fig. 3. From the high frequency side of the spectrum, the bands would be related to organic compounds and adsorbed water content, no organic residues are present but at 3438 cm^{-1} the stretching band of O-H band is complemented with the related bending band of O-H in 1640 cm^{-1} which is attributed to minor absorption of moisture from the atmosphere after calcination [39]. Ti-O-Ti stretching band would have been seen at about 1416 cm^{-1} which would have been related to phase impurities [40]; but its presence is insignificant. In the low frequency region of the spectrum on the other hand, bands related to Nb=O appear at 950 cm^{-1} and Nb-O bond stretching can be seen in 924 cm^{-1} [41]. The stretching band of Ti-O bond is clearly seen in 520 cm^{-1} [42]. In the case of F127-TNO and Cell-TNO samples no bands in the region related to carbon containing moieties are present in the FTIR spectra [43].

Studies on the electrochemical performance of $TiNb_2O_7$ among other niobium-based oxides have shown that nanostructuring may have a minute benefit (if any) in the final performance of the battery compared to other factors related to electrode manufacturing [10, 44, 45]. Although the lithiation potential of TNO is 1.64 V *vs.* Li^+/Li^0, SEI formation and gas evolution has been observed especially in full-cell configurations; these phenomena are exacerbated

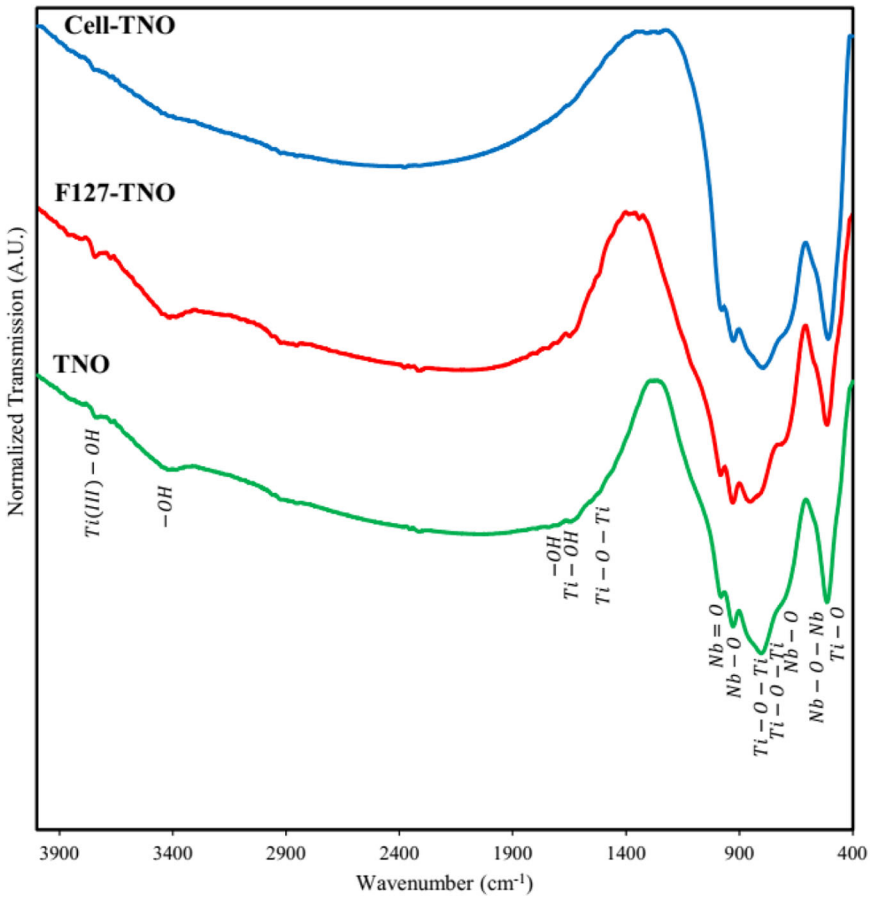

Fig. 3 ATR-FTIR spectra of the samples, peaks are assigned based on the literature

with excessive contact between solid surface and electrolyte [46].

On the other hand, porous TNOs have shown promising results [27, 30, 31, 33]; the benefits of porous structures for enhancing the electrochemical performance of the final electrode can be categorized into three categories. Firstly, an intertwined morphology may facilitate electron and lithium ion conduction which is challenging (especially for electrons in the initial stages of lithiation [10]). Secondly, there is a tradeoff between SEI formation and suitable accessibility to the electrolyte. In ideal conditions, minimal SEI formation would be reimbursed by faster lithium migration and smaller diffusion distances without drying-out of the electrolyte. Thirdly, the interarticular voids formed by porous structures may compensate the volumetric changes related to lithiation (especially in potentials lower than 1 V *vs*. Li^+/Li^0), hence keeping the structural integrity of active electrode layer intact, enhancing the electrochemical performance in extended cycles.

The morphology of the samples under study was investigated by field-emission scanning electron microscopy, the results of which are presented in Fig. 4. With the aim of maximizing the aforementioned benefits related to porous structures while mitigating the issues related to excessive SEI formation, the samples under study were chosen from a variety of other candidates for further electrochemical testing. An irregular morphology with structural features in the scale of hundreds of nanometers in the case of "TNO" sample was chosen as control, by using an appropriate ratio of F127 as structure directing agent, hierarchical morphology consisting of interconnected particles in the scale range of hundreds of nanometers can be formed in the case of "F127-TNO" sample. And finally, by using cellulose from tissue paper as sacrificial soft template, a hierarchy with larger morphological voids in the micron scale can be formed in the case of "Cell-TNO" sample as can be inferred from Fig. 4e.

To further elucidate the morphological and crystallographic features, TNO and Cell-TNO samples were also investigated with TEM/HRTEM and selected area electron diffraction patterns (SAD), the results of which are presented in Fig. 5. As can be deduced from the aforementioned micrographs, without using any template/structure directing agent, the evaporative sol-gel approach yields highly crystalline irregularly shaped particles in tens of nanometers size scale. The lattice image (Fig. 5b) for this sample shows minimal crystalline defects and imperfections (including dislocations) which is well-suited for hindering

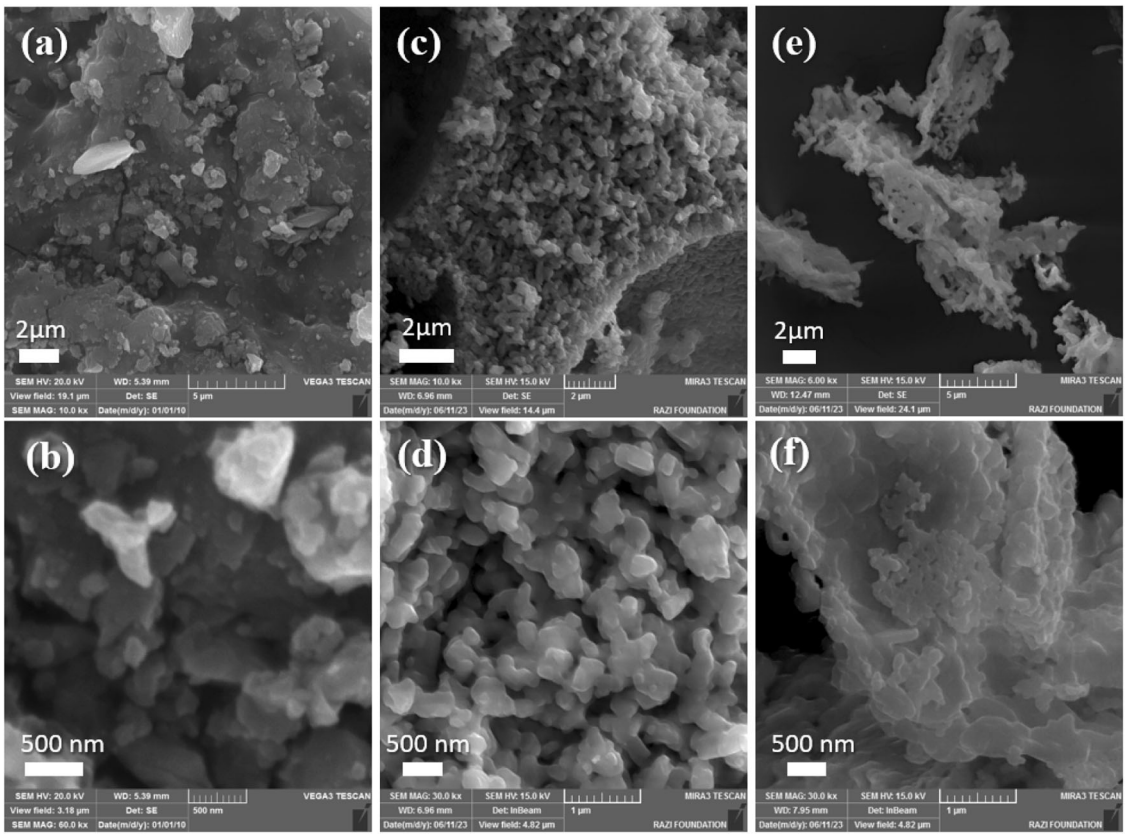

Fig. 4 Field-emission scanning electron micrographs of the samples under study (**a**, **b**: TNO, **c**, **d**: F127-TNO and **e**, **f**: Cell-TNO) in different magnifications showing significant microstructural changes based on the utilized templating approach

irreversible lithiation and capacity loss during cycling. On the other hand, for Cell-TNO sample the morphological features are very different. By using cellulose fibers as hard template, much smaller particles in a few nanometers size scale and high crystallinity are formed which can improve interfacial phenomena and surface diffusion. The SAD pattern of Fig. 5f shows well defined Airy disks which are characteristic of nanocrystalline particles with a statistically variant crystalline orientation.

Based on characterization data, the synthesis steps and resulting morphological features (in terms of particulate size and interarticular pores are schematically presented in Fig. 6. The chemical reactions taking place in the synthesis can be divided into alcoholysis which removes the butyl moieties from titanium butoxide and then polycondensation of mixed titanium and niobium species into a gel network with random distribution of both metallic elements and oxygen linkers. Upon high temperature calcination and annealing to room temperature, the aforementioned gel network would transform into the monoclinic crystal of $TiNb_2O_7$ (see Fig. 1a).

As mentioned before, the crystalline voids in the monoclinic unit-cell of TNO can reversibly accommodate lithium ions upon cycling. A high degree of crystallinity with larger particulates would decrease the amount of grain boundaries and free surface imperfections. In such conditions, lithium ions will have an ordered host crystal with only Li^+ bulk diffusion controlling the amount that can be accommodated. On the other hand, TNO is a wide band-gap semiconductor (Eg~3 eV as measured from extrapolation of Tauc plots) and its electrical and ionic conduction can be seen as hinderance factors especially for high-rate performance in lithiation cycles. Smaller particles (to a certain extent) with a proper distribution of interarticular porosity are proven to be beneficial in enhancing the interfacial contact between the active solid particles in electrode and the Li^+ containing electrolyte. Furthermore, it should be noted that unlike LTO, titanium niobates do express certain volumetric changes upon lithiation, which indeed leads to poor cycling performance and loss of active material from the electrode. Introduction of irregular porosity is postulated to have a damping effect mitigating the loss of electrical contact between active material particles and electrode upon consecutive cycling. Abovementioned hypothesis was put to test by electrochemically cycling the samples under study against lithium metal in a half-cell configuration.

The electrochemical performance of the samples under study at different current density values calculated based on the theoretical capacity of 387.6 $mAhg^{-1}$ for TNO and the

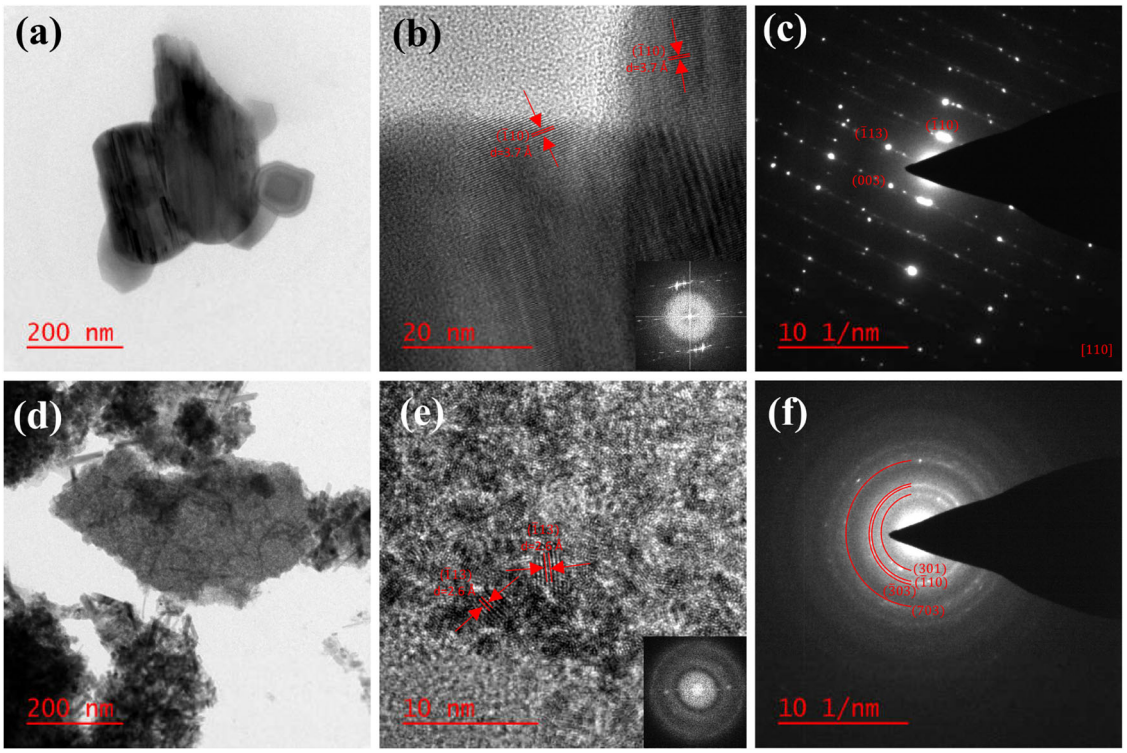

Fig. 5 Transmission electron micrographs of the samples under study (**a**, **b**: TNO and **d**, **e**: Cell-TNO). The insert of parts "**b**" and "**e**" represent the FFT of each respective lattice image. Parts "**c**" and "**f**" show the SAD patterns of the samples TNO and Cell-TNO, respectively

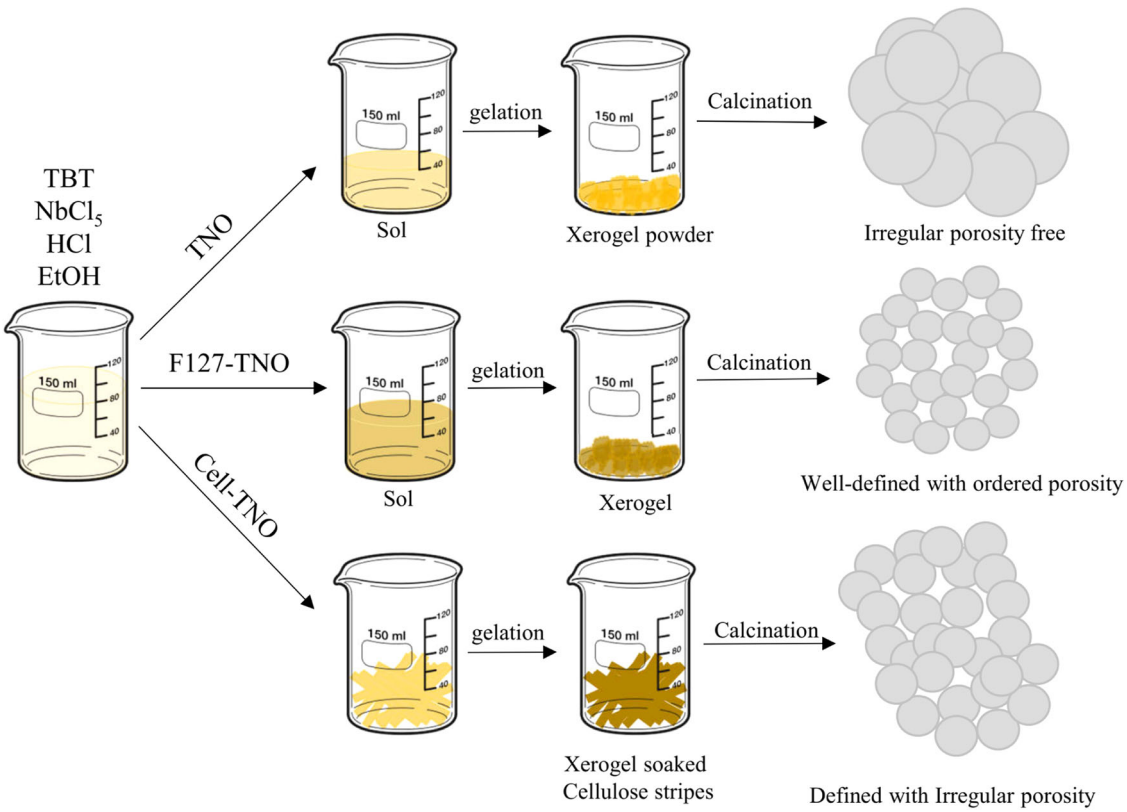

Fig. 6 Schematic representation of synthesis conditions and resultant morphologies for the samples under study

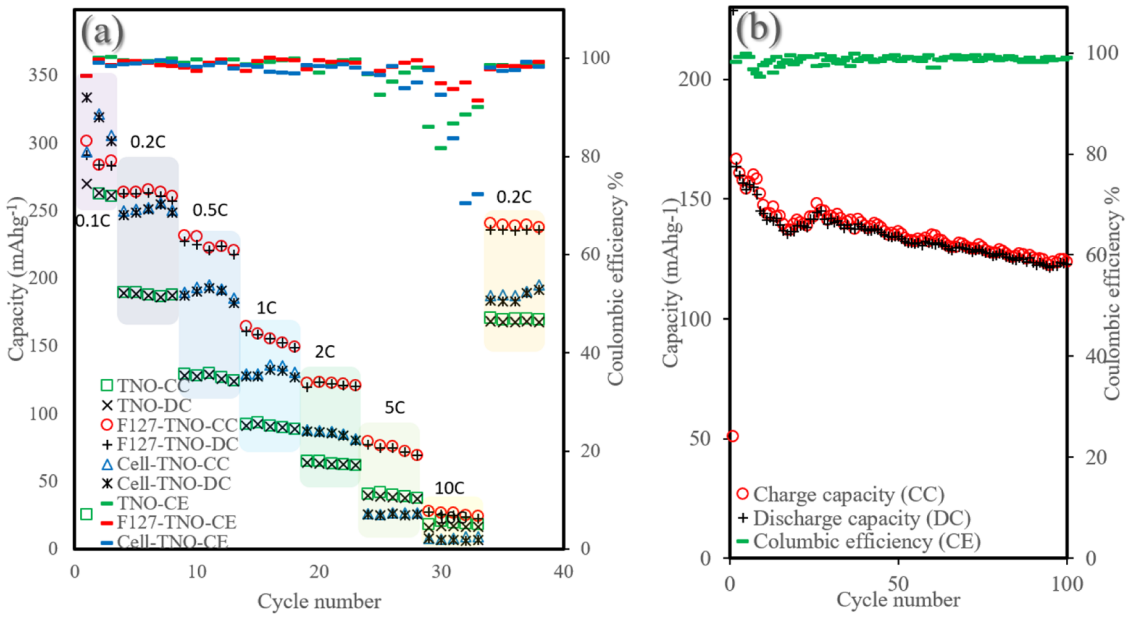

Fig. 7 Electrochemical performance of the samples under study in half cell configuration; **a** rate performance of samples TNO, F127-TNO and Cell-TNO at different rates of charge and discharge (calculated from the theoretical capacity of 387.6 $mAhg^{-1}$ for pure $TiNb_2O_7$ phase). **b** Cycling performance of F127-TNO sample showing more than 76% capacity retention after 100 cycles of charge/discharge at constant rate of 1C

Table 2 Summary of crystallographic properties and battery testing results for the samples under study

Sample	D (nm)	$\varepsilon \times 10^3$	R (nm)	$\delta \times 10^3$ (nm^{-2})	1C capacity ($mAhg^{-1}$)	Initial CE (%)
TNO	21.59	7.67	0.4650	2.15	90	99.8
F127-TNO	17.85	9.28	0.4653	3.14	155	99.2
Cell-TNO	23.01	7.19	0.4649	1.89	132	99.2

Crystallite size, $D = \frac{k\lambda}{L\cos\theta}$; micro strain, $\varepsilon = \frac{L}{4\tan\theta}$; average inner crystalline separation, $R = \frac{5\lambda}{8\sin\theta}$; dislocation density, $\delta = \frac{1}{D^2}$; while k: Scherrer's constant, λ = X-ray wavelength, L = FWHM in radians and θ: Bragg diffraction angle

amount of active material in each half-cell are presented in Fig. 7 and Table 2. As can be deduced from part "a" of Fig. 7, the performance of "TNO" sample is inferior to both "F127-TNO" and "Cell-TNO" samples in all current density values. In the case of "Cell-TNO" sample, although the capacity in low current density values is promising (even surpassing 300 $mAhg^{-1}$ at 0.1 C rate), the performance declines markedly especially at rates higher than 0.5 C. At even higher rates (5 C and 10 C) the performance of "Cell-TNO" sample becomes even worse than that of "TNO" sample, suggesting the formation of SEI which manifests itself with lowered columbic efficiency at these steps as well. The performance of "F127-TNO" sample is superior to other samples under study in virtually all of the rates under study suggesting the optimized morphology for electrochemical performance. Furthermore, this sample was put through cycling test at 1 C for 100 consecutive charge/discharge regimes and showed a capacity retention of more than 76% based on the first cycle at the same rate (it should be noted that the first cycle in Fig. 7b was performed in low rate for a fresh half-cell). Actual capacity values are highly dependent upon non-material aspects of electrode processing i.e., conductive additives for the slurry, electrolyte additives, electrode calendaring and mass loading. Best efforts were spent on keeping the such parameters as uniform as possible amongst the samples under study to validate the comparison.

Based on the (110) reflection which presents itself at about $2\theta = 23.9°$ and peak broadening in terms of full-width at half-maximum (FWHM) it is possible to calculate crystalline parameters such as crystallite size, micro strain, average inner-crystalline separation and dislocation density. These parameters are presented in Table 2 in comparison. It is evident that "F127-TNO has the smallest crystallite size in the series of samples under study which is coupled with an expected increase in micro strain and higher density of dislocations. However, this sample shows the highest capacity when tested in all of the current density values except for 0.1 C; this may be attributed to the increased contact between the solid active material and electrolyte due to higher surface area. On the other hand, at the lowest current density value of 0.1 C, the timescale for ion mobility and diffusion does not determine the overall performance of the electrode, rather, the sample with largest crystallites, lowest macro strain and lowest density of dislocations shows better performance.

4 Conclusions

A series of TNO-based nanostructures as anode materials in Li-ion batteries were synthesized *via* evaporative sol-gel approach. Several logical criteria for screening candidates (in terms of phase content and morphological aspects) were presented based on fundamental literature. Based on the presented criteria, there samples were chosen for electrochemical testing. These samples clearly demonstrate the effect of two templating agents (F127 as a representative soft template and cellulose as a representative sacrificial hard template) on the phase, crystallite parameters (e.g., preferential growth) and morphology of the final ceramic. Electrochemical performance at a desired current density value is determined by a delicate balance between several parameters some of which are even self-contradicting. Thus, logical compromises should be made for the intended application. Most modern mobility applications rely upon high-rate, highly cyclable batteries and material considerations are crucial for answering such high demands, although necessary, making an optimized active material may not be enough for obtaining an optimized cell. Further studies are underway by our research group in order to comprehensively investigate the parameters related to both material characteristics and electrode production parameters of this interesting material.

Acknowledgements The authors wish to thank KNTU and Iran Nanotechnology Innovation Council for financial support.

Author contributions ARR has synthesized the materials, fabricated the electrode materials, wrote the whole manuscript including tables and figures, and performed all the calculations. MKH was the supervisor who guided and supported all the time regarding the data collection, analysis, and presentation.

Compliance with ethical standards

Conflict of interest The authors declare no conflict of interest.

References

1. Ozawa K (2012) Lithium ion rechargeable batteries: materials, technology, and new applications. John Wiley & Sons. Wiley VCH Verlag, Weinheim, Germany. https://www.wiley.com/enhk/Lithium+Ion+Rechargeable+Batteries%3A+Materials%2C+Technology%2C+and+New+Applications-p-9783527319831
2. Nzereogu P, Omah A, Ezema F, Iwuoha E, Nwanya A (2022) Anode materials for lithium-ion batteries: A review. Appl Surf Sci Adv 9:100233
3. Deng J, Bae C, Denlinger A, Miller T (2020) Electric vehicles batteries: requirements and challenges. Joule 4(3):511–515
4. Cheng J-H, Assegie AA, Huang C-J, Lin M-H, Tripathi AM, Wang C-C, Tang M-T, Song Y-F, Su W-N, Hwang BJ (2017) Visualization of lithium plating and stripping via in operando transmission X-ray microscopy. J Phys Chem C 121(14):7761–7766
5. Finegan DP, Darcy E, Keyser M, Tjaden B, Heenan TM, Jervis R, Bailey JJ, Malik R, Vo NT, Magdysyuk OV (2017) Characterising thermal runaway within lithium-ion cells by inducing and monitoring internal short circuits. Energy Environ Sci 10(6):1377–1388
6. Shi H, Shi C, Jia Z, Zhang L, Wang H, Chen J (2022) Titanium dioxide-based anode materials for lithium-ion batteries: structure and synthesis. RSC Adv 12(52):33641–33652
7. Zhang H, Yang Y, Xu H, Wang L, Lu X, He X (2022) Li4Ti5O12 spinel anode: Fundamentals and advances in rechargeable batteries. InfoMat 4(4):e12228
8. Ezhyeh ZN, Khodaei M, Torabi F (2023) Review on doping strategy in Li4Ti5O12 as an anode material for Lithium-ion batteries. Ceram Int 49(5):7105–7141. https://doi.org/10.1016/j.ceramint.2022.04.340
9. Han J-T, Huang Y-H, Goodenough JB (2011) New anode framework for rechargeable lithium batteries. Chem Mater 23(8):2027–2029
10. Griffith KJ, Seymour ID, Hope MA, Butala MM, Lamontagne LK, Preefer MB, Koçer CP, Henkelman G, Morris AJ, Cliffe MJ (2019) Ionic and electronic conduction in TiNb2O7. J Am Chem Soc 141(42):16706–16725
11. Griffith KJ, Senyshyn A, Grey CP (2017) Structural stability from crystallographic shear in TiO2–Nb2O5 phases: Cation ordering and lithiation behavior of TiNb24O62. Inorg Chem 56(7):4002–4010
12. Lu X, Jian Z, Fang Z, Gu L, Hu Y-S, Chen W, Wang Z, Chen L (2011) Atomic-scale investigation on lithium storage mechanism in TiNb 2 O 7. Energy Environ Sci 4(8):2638–2644
13. Aghamohammadi H, Hassanzadeh N, Eslami-Farsani R (2022) A comprehensive review study on pure titanium niobium oxide as the anode material for Li-ion batteries. J Alloy Compd 911:165117. https://doi.org/10.1016/j.jallcom.2022.165117
14. Aghamohammadi H, Hassanzadeh N, Eslami-Farsani R (2021) A review study on titanium niobium oxide-based composite anodes for Li-ion batteries: Synthesis, structure, and performance. Ceram Int 47(19):26598–26619. https://doi.org/10.1016/j.ceramint.2021.06.127
15. Aghamohammadi H, Eslami-Farsani R (2022) Synthesis and electrochemical performance of TiNb2O7 nanoparticles grown on electrochemically prepared graphene as anode materials for Li-ion batteries. J Power Sources 535:231418. https://doi.org/10.1016/j.jpowsour.2022.231418
16. Tian T, Lu LL, Yin YC, Li F, Zhang TW, Song YH, Tan YH, Yao HB (2021) Multiscale designed niobium titanium oxide anode for fast charging lithium ion batteries. Adv Funct Mater 31(4):2007419
17. Zhu W, Zou B, Zhang C, Ng DH, El-Khodary SA, Liu X, Li G, Qiu J, Zhao Y, Yang S (2020) Oxygen-Defective TiNb2O7-x Nanochains with Enlarged Lattice Spacing for High-Rate Lithium Ion Capacitor. Adv Mater Interfaces 7(16):2000705
18. Inada R, Mori T, Kumasaka R, Ito R, Tojo T, Sakurai Y (2019) Characterization of vacuum-annealed TiNb2O7 as high potential anode material for lithium-ion battery. Int J Appl Ceram Technol 16(1):264–272
19. Gao J, Cheng X, Lou S, Ma Y, Zuo P, Du C, Gao Y, Yin G (2017) Self-doping Ti1-xNb2+ xO7 anode material for lithium-ion battery and its electrochemical performance. J Alloy Compd 728:534–540
20. Liu K, Wang J-a, Yang J, Zhao D, Chen P, Man J, Yu X, Wen Z, Sun J (2021) Interstitial and substitutional V5+-doped TiNb2O7 microspheres: A novel doping way to achieve high-performance electrodes. Chem Eng J 407:127190
21. Wen X, Ma C, Du C, Liu J, Zhang X, Qu D, Tang Z (2015) Enhanced electrochemical properties of vanadium-doped titanium

niobate as a new anode material for lithium-ion batteries. Electrochim Acta 186:58–63
22. Song H, Kim Y-T (2015) A Mo-doped TiNb 2 O 7 anode for lithium-ion batteries with high rate capability due to charge redistribution. Chem Commun 51(48):9849–9852
23. Lei C, Qin X, Huang S, Wei T, Zhang Y (2021) Mo-Doped TiNb2O7 Microspheres as Improved Anode Materials for Lithium-Ion Batteries. ChemElectroChem 8(17):3379–3383
24. Lin C, Yu S, Wu S, Lin S, Zhu Z-Z, Li J, Lu L (2015) Ru 0.01 Ti 0.99 Nb 2 O 7 as an intercalation-type anode material with a large capacity and high rate performance for lithium-ion batteries. J Mater Chem A 3(16):8627–8635
25. Lou S, Ma Y, Cheng X, Gao J, Gao Y, Zuo P, Du C, Yin G (2015) Facile synthesis of nanostructured TiNb 2 O 7 anode materials with superior performance for high-rate lithium ion batteries. Chem Commun 51(97):17293–17296
26. Thiyagarajan GB, Shanmugam V, Wilhelm M, Mathur S, Moodakare SB, Kumar R (2021) TiNb2O7-Keratin derived carbon nanocomposites as novel anode materials for high-capacity lithium-ion batteries. Open Ceram 6:100131
27. Guo B, Yu X, Sun X-G, Chi M, Qiao Z-A, Liu J, Hu Y-S, Yang X-Q, Goodenough JB, Dai S (2014) A long-life lithium-ion battery with a highly porous TiNb 2 O 7 anode for large-scale electrical energy storage. Energy Environ Sci 7(7):2220–2226
28. Hu L, Lin C, Wang C, Yang C, Li J, Chen Y, Lin S (2016) TiNb2O7 nanorods as a novel anode material for secondary lithium-ion batteries. Funct Mater Lett 9(06):1642004
29. Fei L, Xu Y, Wu X, Li Y, Xie P, Deng S, Smirnov S, Luo H (2013) SBA-15 confined synthesis of TiNb 2 O 7 nanoparticles for lithium-ion batteries. Nanoscale 5(22):11102–11107
30. Li H, Shen L, Wang J, Fang S, Zhang Y, Dou H, Zhang X (2015) Three-dimensionally ordered porous TiNb 2 O 7 nanotubes: A superior anode material for next generation hybrid supercapacitors. J Mater Chem A 3(32):16785–16790
31. Lou S, Cheng X, Zhao Y, Lushington A, Gao J, Li Q, Zuo P, Wang B, Gao Y, Ma Y (2017) Superior performance of ordered macroporous TiNb2O7 anodes for lithium ion batteries: understanding from the structural and pseudocapacitive insights on achieving high rate capability. Nano Energy 34:15–25
32. Li H, Zhang Y, Tang Y, Zhao F, Zhao B, Hu Y, Murat H, Gao S, Liu L (2019) TiNb2O7 nanowires with high electrochemical performances as anodes for lithium ion batteries. Appl Surf Sci 475:942–946
33. Jo C, Kim Y, Hwang J, Shim J, Chun J, Lee J (2014) Block copolymer directed ordered mesostructured TiNb2O7 multimetallic oxide constructed of nanocrystals as high power Li-ion battery anodes. Chem Mater 26(11):3508–3514
34. Aronne A, Marenna E, Califano V, Fanelli E, Pernice P, Trifuoggi M, Vergara A (2007) Sol–gel synthesis and structural characterization of niobium-silicon mixed-oxide nanocomposites. J Sol Gel Sci Technol 43:193–204
35. Lutterotti L, Matthies S, Wenk H (1999) MAUD: a friendly Java program for material analysis using diffraction. CPD Newsletter 21:14–15
36. Harada Y, Takami N, Inagaki H, Yoshida Y (2016) Battery active material, nonaqueous electrolyte battery and battery pack. USA Patent,
37. Tauc J, Grigorovici R, Vancu A (1966) Optical properties and electronic structure of amorphous germanium. Phys Status Solidi 15(2):627–637
38. Makuła P, Pacia M, Macyk W (2018) How to correctly determine the band gap energy of modified semiconductor photocatalysts based on UV–Vis spectra. J Phys Chem Lett 9(23):6814–6817
39. Chougala L, Yatnatti M, Linganagoudar R, Kamble R, Kadadevarmath J (2017) A simple approach on synthesis of TiO2 nanoparticles and its application in dye sensitized solar cells. J Nano Electron Phys 9(4):4005–4001
40. Al-Oubidy EA, Kadhim FJ (2019) Photocatalytic activity of anatase titanium dioxide nanostructures prepared by reactive magnetron sputtering technique. Optical Quantum Electron 51(1):23
41. Qaraah FA, Mahyoub SA, Hafez ME, Xiu G (2019) Facile route for C–N/Nb 2 O 5 nanonet synthesis based on 2-methylimidazole for visible-light driven photocatalytic degradation of Rhodamine B. RSC Adv 9(68):39561–39571
42. Mirabedini A, Mirabedini S, Babalou A, Pazokifard S (2011) Synthesis, characterization and enhanced photocatalytic activity of TiO2/SiO2 nanocomposite in an aqueous solution and acrylic-based coatings. Prog Org Coat 72(3):453–460
43. Abderrahim B, Abderrahman E, Mohamed A, Fatima T, Abdesselam T, Krim O (2015) Kinetic thermal degradation of cellulose, polybutylene succinate and a green composite: comparative study. World J Environ Eng 3(4):95–110
44. Griffith KJ, Wiaderek KM, Cibin G, Marbella LE, Grey CP (2018) Niobium tungsten oxides for high-rate lithium-ion energy storage. Nature 559(7715):556–563
45. Griffith KJ, Forse AC, Griffin JM, Grey CP (2016) High-rate intercalation without nanostructuring in metastable Nb2O5 bronze phases. J Am Chem Soc 138(28):8888–8899
46. Wu X, Lou S, Cheng X, Lin C, Gao J, Ma Y, Zuo P, Du C, Gao Y, Yin G (2018) Unravelling the interface layer formation and gas evolution/suppression on a TiNb2O7 anode for lithium-ion batteries. ACS Appl Mater interfaces 10(32):27056–27062